Climate change linked to drought in Southern Madagascar

Angela Rigden[1*], Christopher Golden[2], Duo Chan[3] and Peter Huybers[4]

[1*]Department of Earth System Science, University of California, Irvine, 3200 Croul Hall St, Irvine, 92697, CA, USA.
[2]Department of Nutrition, Harvard T.H. Chan School of Public Health, 677 Huntington Ave, Boston, 02115, MA, USA.
[3]School of Ocean and Earth Science, University of Southampton, European Way, Southampton, S014 3ZH, Hampshire, UK.
[4]Department of Earth and Planetary Sciences, Harvard University, 20 Oxford St, Cambridge, 02138, MA, USA.

*Corresponding author(s). E-mail(s): arigden@uci.edu;
Contributing authors: golden@hsph.harvard.edu;
Duo.Chan@soton.ac.uk; phuybers@fas.harvard.edu;

Keywords: drought, climate change, climate change attribution, hydrology, remote sensing

1 Supplementary Methods

1.1 Precipitation gauges in Madagascar

Precipitation gauges used as input to the CHIRPS dataset [4] are mapped across Madagascar with the completeness of the record indicated for each gauge as the fraction of months available from 1982 to 2022 (Supplementary Fig. 1). There are three precipitation gauges in Southern Madagascar: Fort Dauphin, Tulear, and Morombe. Note that we define Southern Madagascar as the three most southern political regions: Atsimo-Andrefana, Androy, and Anosy. Fort Dauphine has 60% of the months from 1982 to 2022, Tulear has 65%, and Morombe, 26%. All three gauges are in close proximity to the coast, with Fort Dauphin in the south east of the Anosy Region, Tulear in the central-west of the Atsimo-Andrefana Region, and Morombre in the north-west of the Atsimo-Andrefana Region.

1.2 Climate model simulations

We utilize two variables from CMIP6, vertical velocity and soil moisture, each of which is discussed below.

1.2.1 Vertical velocity

Changes in atmospheric circulation over Madagascar are explored using zonally averaged (39.5-59.5°E) monthly vertical velocity at 500 hPa from 46 climate models (267 total ensembles; Supplementary Table 1) from 2015 to 2099 (future projections; SSP5-8.5).

Fig. 3a shows the latitude of maximum vertical velocity in the Southern Hemisphere (<-15°S) and Northern Hemisphere (>15°N), and an estimate of the trend in the latitude of maximum vertical velocity using a linear least-squares regression. Fig. 3b shows the trend in the maximum vertical velocity, again, from linear least-squares regression.

The trend in the maximum vertical velocity position and intensity is similar when using only the nine model runs we focus on (Supplementary Table 1) relative to using all 267 ensembles (Supplementary Fig. 3 includes nine models; Fig. 3 includes all 267 ensembles).

1.2.2 Soil moisture

We qualitatively assess climate model output from the CMIP6 by examining seasonality (Supplementary Fig. 4) and spatial patterns (Supplementary Fig. 5). Our criteria for inclusion includes: (1) realistic seasonality of soil moisture that peaks in the Austral summer and (2) spatial patterns of soil moisture that exhibit drier conditions, on average, in Southern Madagascar relative to the central and northern regions.

1.3 Climate change fingerprint

We repeat the analysis for Fig. 2a using data from 1982 to 2022 (Supplementary Fig. 7) and Fig. 2a-b using seasonal data (Supplementary Fig. 8). We also repeat climate change fingerprint analysis using precipitation observations from CHIRPS [4] and CMIP6 simulations.

1.4 Attribution of long-term trends and drought

We represent the distribution of long-term trends across seasons using a multivariate normal (MVN) distribution. Our approach is based on foregoing studies that use model simulations with and without anthropogenic forcing to establish if observed conditions are due to anthropogenic forcing (e.g. [47]). We extend upon this model-comparison approach by jointly analyzing the pattern of all seasonal trends, rather than focusing on one season. Our approach is similar to other recent studies that use multivariate techniques to attribute climate change in the context of compound extremes, for example, driven by temperature and precipitation [48].

An MVN distribution is specified in terms of the mean trends for each season (μ) and the covariance among seasonal trends (Σ),

$$L(x) = \frac{1}{\sqrt{|\Sigma|(2\pi)^d}} \exp\left(-\frac{1}{2}(x-\mu)\Sigma^{-1}(x-\mu)'\right), \tag{A1}$$

where x and μ are 1-by-d vectors, Σ is a d-by-d symmetric, positive definite matrix, and $|\Sigma|$ represents the determinant. There are $d = 4$ seasons (SON, DJF, MAM, and JJA). Σ is estimated as a robust covariance, which is less sensitive to outliers than an empirical covariance, using the FAST-minimum covariance determinant algorithm with an outlier fraction set to 0.25 of the data [49], and μ is estimated as the robust minimum covariance determinant mean.

An MVN distribution is fit using robust methods to 819 realizations of seasonal trends from the control simulations (L_{null} in Supplementary Table 2). Another MVN distribution is fit to nine realizations of seasonal trends from the forced simulations using an empirical covariance and empirical mean (L_{alt} "Alt 1" in Supplementary Table 2). The control simulations characterize the null distribution of internal variability in soil moisture trends, whereas the forced simulations characterize an alternate distribution of forced trends in soil moisture. Note that the number of trend realizations from the control simulations is more than the forced simulations because the control simulations are run for 500 years, while we only use the nine trends from 1982 to 2022 in the forced simulations. Slices of the four dimensional MVN distributions show that trends covary across seasons in the simulations. For example, the forced simulations show a clear positive covariance between trends in JJA and SON, as demonstrated by the long axis of the covariance ellipsoid (Supplementary Fig. 16c).

The observed proxy seasonal trends, x, are assessed conditional on the forced alternate distributions relative to the control null distribution, giving a likelihood ratio $\lambda = L_{\text{alt}}(x)/L_{\text{null}}(x)$. For purposes of uncertainty quantification, MVN distributions are repeatedly fit using a bootstrapping approach. For each of 1000 iterations, we evaluate λ at a sample of x, analogous to those obtained from the distribution of bootstrapped trends used to estimate the confidence intervals in Fig. 8b. A 90% confidence interval is indicated for the likelihood ratios as the 5% and 95% percentiles that reflect both the uncertainties in the fit distributions (μ, Σ) and proxy soil moisture trends (x), which are re-estimated from a sample of years with replacement for each fit of the MVN distributions.

We find that the observed seasonal trend pattern in proxy soil moisture is 100 times more likely to occur in the forced simulations relative to the control simulations, or $\lambda = 100$, with a 90% confidence interval of 5–2683. Slices of the MVN distributions illustrate this result, with x falling within the MVN from forced simulations ($p<0.1$) and outside the MVN from the control simulations ($p>0.1$) (Supplementary Fig. 16).

The MVN distribution representing the forced conditions is fit to only a small sample size of 9 realizations. To evaluate if our results are sensitive to this small sample size we generate two other sets of samples, both of which allow for the estimation of the covariance and mean using robust methods. First, we fit a MVN distribution to a set of 18 realizations from the forced simulations, with 9 spanning 1982 to 2022 and 9 spanning 1987 to 2027 ("Alt 2" Supplementary

Table 2). This fit gives $\lambda = 164$ (90% CI: 19-2754 times). Secondly, we fit the alternative MVN distribution to a set of 144 trends over the epoch 1982–2099, or 118 years, from the forced simulations ("Alt 3" Supplementary Table 2). Here, we assume that 41-year trends estimated over the 1982-2099 period are sufficiently similar to the subset of earlier trends, which is supported by a relatively linear soil moisture trend in the forced simulations over this period (Supplementary Fig. 6). Using this alternative distribution, we obtain $\lambda = 126$ (90% CI: 21-1387 times), such that both alternate methods of estimating λ are consistent with our main result.

We next turn to assessing whether the observed trends in soil moisture made the droughts observed between 2017–2022 more likely. To determine if these droughts are attributable to anthropogenic forcing, we use MVN distributions to represent seasonal soil moisture anomalies.

Approach 1: In our main approach, the MVN distribution is specified in terms of seasonal soil moisture anomalies (μ) and the covariance among seasonal anomalies (Σ) using two different intervals from forced simulations. We use time separation, as opposed to control-model simulations, for purposes of attribution of anthropogenic forcing because this better allows for comparison against historical observations.

An MVN is fit to 270 realizations of seasonal anomalies from a historical period in the forced simulations, L_{null}, and a second time to 270 realizations of seasonal anomalies from a current period in the forced simulations, L_{alt}. Note that we use soil moisture anomalies, as opposed to magnitudes, because mean soil moisture levels vary greatly between CMIP6 models [45]. A baseline period is specified as the 30-year period from 1970–1999, and a current period is taken as 2005–2034, or a 30-year interval centered on the recent droughts. Anomalies are estimated for each period and model by subtracting the seasonal average conditions during the baseline period. We then evaluate the likelihood of the observed anomalies during the drought, x, for the baseline and current MVN distribution. Observational anomalies x are computed by removing the value predicted for 1982 from a least-squares linear fit to pre-drought soil moisture over 1982-2017.

Likelihood ratios are obtained for each year of the drought as $\lambda_y = L_{alt}(x_y)/L_{null}(x_y)$. An overall likelihood ratio for the observed droughts is obtained by multiplying the individual ratios, $\lambda_o = \prod_y \lambda_y$. Slices of the four dimensional MVN distributions and associated x_y values for all drought years are shown in Supplementary Fig. 17. Values for λ_y are also obtained evaluating L_{alt} for different 30-year intervals over the period 2000-2099 at 5-year increments (Fig. 5)

Approach 2: In approach 2, we modify the input data such that the MVN distributions for the baseline period (1970-1999; x_{null} in Supplementary Table 2) and recent period (e.g. centered on the drought years from 2005-2034; x_{null} in Supplementary Table 2) are fit based on the observed trend in proxy soil moisture. Specifically, we use the covariance from approach 1 but update mean values using the baseline and drought conditions predicted from a linear regression in proxy soil moisture from 1982 to 2017. Of most relevance, whereas the forced climate simulations only indicate drying of 0.0022 cm^3 cm^{-3} decade^{-1} (median across climate models) between 1982 and 2017 during the onset of the rainy season, the observations indicate that the drying is over twice this magnitude (0.0055 cm^3 cm^{-3} decade^{-1}). The baseline mean is set to the predicted 1982 conditions and the future mean is set to the extrapolation of the trend for each drought year. Note that we do not fit MVN distributions over a long range of future periods, as in approach 1, since the mean of the MVN distributions are derived from the observed trend in proxy soil moisture, and extrapolation of these trends may not well represent the future. Likelihoods ratios are evaluated at the seasonal proxy soil moisture values observed for each year of the drought as $\lambda_y = L_{alt}(x_y)/L_{null}(x_y)$.

For both drought attribution approaches, uncertainty in the MVN distributions are quantified using a bootstrapping approach. For each of 1000 iterations, the linear trend in proxy soil moisture from 1982 to 2017 (used in the estimating anomalies x in approach 1 and μ in approach 2) is estimated from a sample of the years from 1982-2017 with replacement. A 90% confidence interval is indicated for the likelihood ratios as the 5% and 95% percentiles, and reflect both the uncertainties in the fit distributions and the estimation of the linear trend in proxy soil moisture from 1982-2017.

Using either approach, we find that the drought conditions are significantly more likely in current than the baseline periods (Supplementary Table 3). Using approach 1, we find that the drought conditions observed from 2017 to 2022 are 15 times (90% CI: 8-27 times) more likely to occur in 2005-2034 than in 1970-1999. Furthermore, future climate change is expected to further increases the probability of the observed drought conditions with the observed drought conditions >1000 times (90% CI: >1000 times) more likely to occur in 2070-2099 relative to 1970-1999. This results is visually apparent in the slices of the MVN distributions, as the observed conditions are more consistent with the MVN in the 2070-2090 conditions relative to the 1970-1999 conditions (Supplementary Fig. 17a). Approach 2 indicates a higher likelihood ratio than approach 1 giving further support to anthropogenic forcing making the droughts more likely. This follows from the trends in the observed proxy soil moisture generally being larger than simulated trends.

2 Supplementary Figures

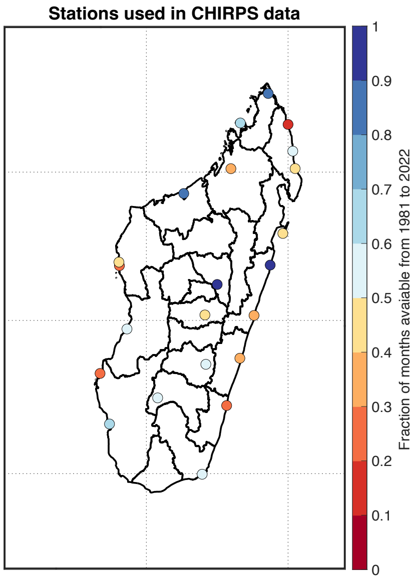

Supplementary Figure 1 Precipitation gauges used in the CHIRPS dataset Gauges are colored by the data availability of monthly reports from 1982 to 2022. Note that the three stations in Southern Madagascar, i.e. the three most Southern Regions, have the following data available: Tulear (0.65), Fort Dauphin (0.60), and Morombe (0.26).

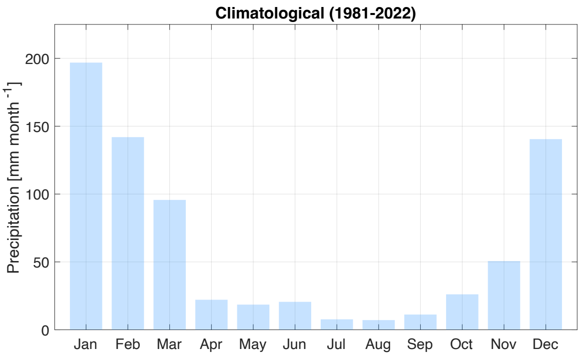

Supplementary Figure 2 Monthly precipitation Average monthly precipitation over Southern Madagascar from 1981 to 2022 from CHIRPS.

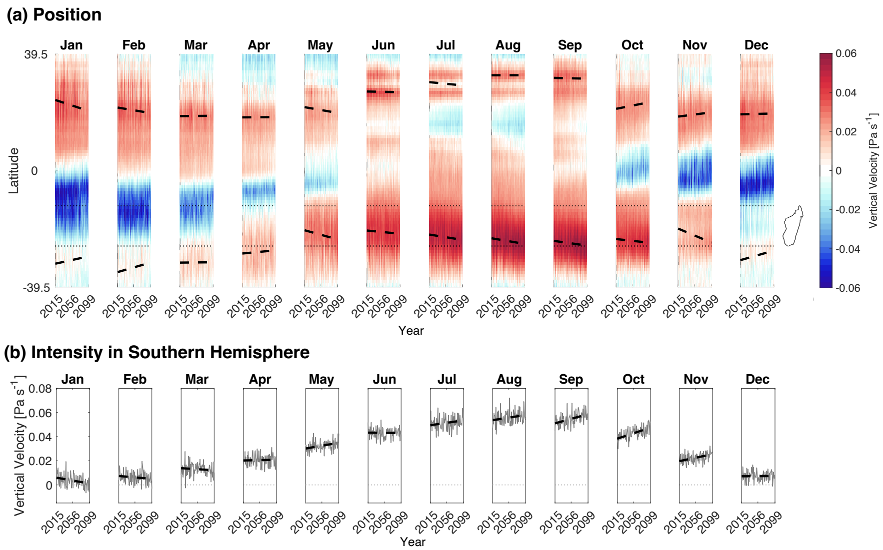

Supplementary Figure 3 Projected changes in atmospheric circulation Same as Fig. 3, but using only the nine model runs from the main analyses (see Supplementary Table 1).

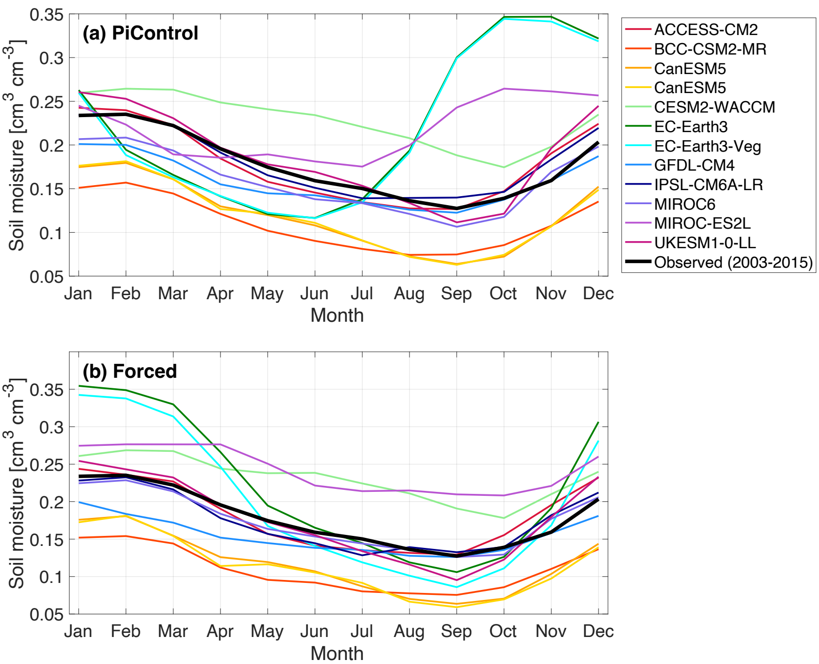

Supplementary Figure 4 Simulated soil moisture seasonality Monthly average soil moisture in the (a) piControl (years 1-500) and (b) forced (1990-2020) simulations from twelve CMIP6 models. EC-Earth3-Veg, EC-Earth3, and MIROC-ES2L are excluded from the attribution analyses on the basis of showing unrealistic seasonal cycles in the pre-industrial control simulations. Observations from 2003 to 2015 (same as shown in Fig. 1d) are included for reference.

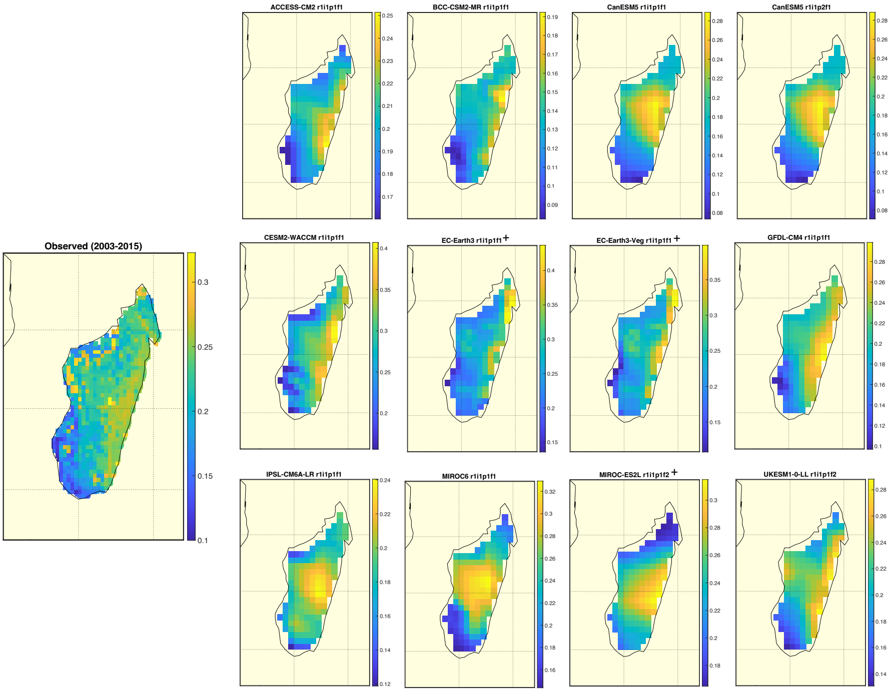

Supplementary Figure 5 Simulated soil moisture spatial patterns Annual average soil moisture (cm^3 cm^{-3}) from 1990-2020 for twelve CMIP6 models. Three of the runs, which are indicated with a plus sign (+) in the titles, are excluded from the analysis because of biases in the seasonal cycle of the piControl simulations. Observations from 2003 to 2015 (same as shown in Fig. 1b) are included in the left plot for reference.

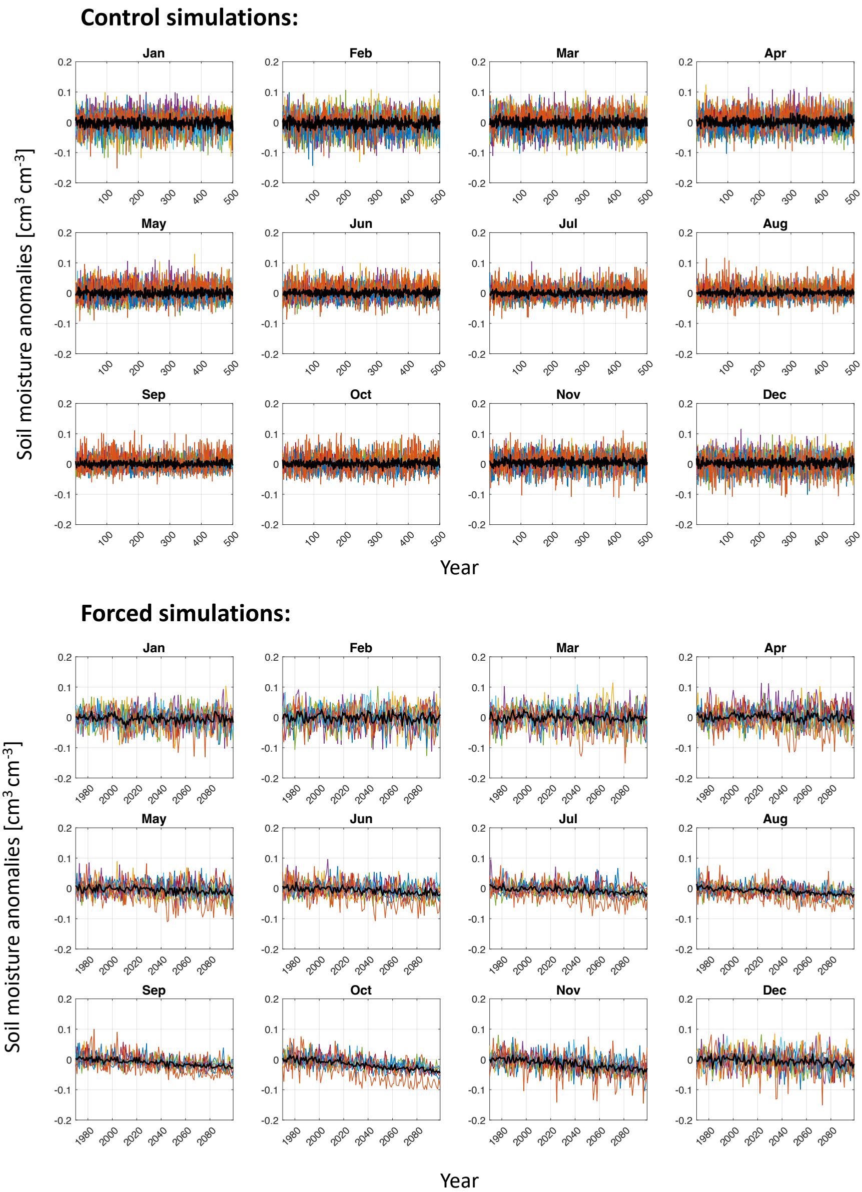

Supplementary Figure 6 Time series of simulated soil moisture anomalies Monthly soil moisture anomalies from the piControl simulations (top 12 panels) and forced simulations (bottom 12 panels) from the nine selected model ensembles (colored lines). The median across models is shown in black. Anomalies are estimate for each model, with the piControl simulations relative to the first 100 years and the forced simulations relative to the 1970-1999 period.

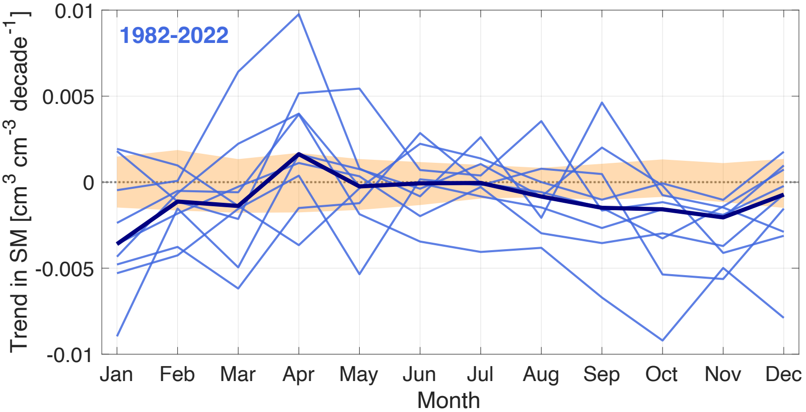

Supplementary Figure 7 Climate change fingerprint Same as Fig. 2a, but trends in the forced simulations are from 1982 to 2022.

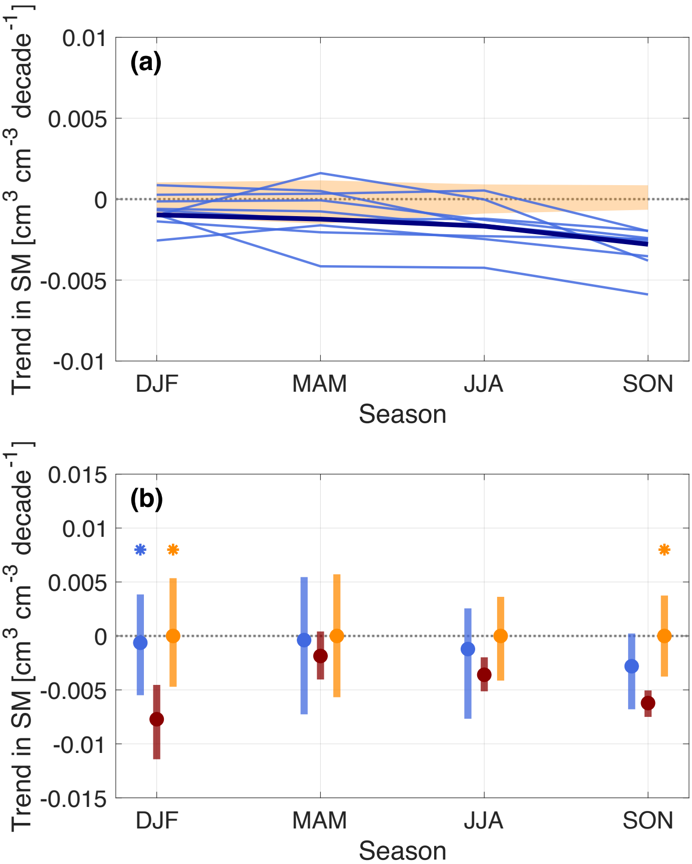

Supplementary Figure 8 Climate change fingerprint Same as Fig. 2, but by season.

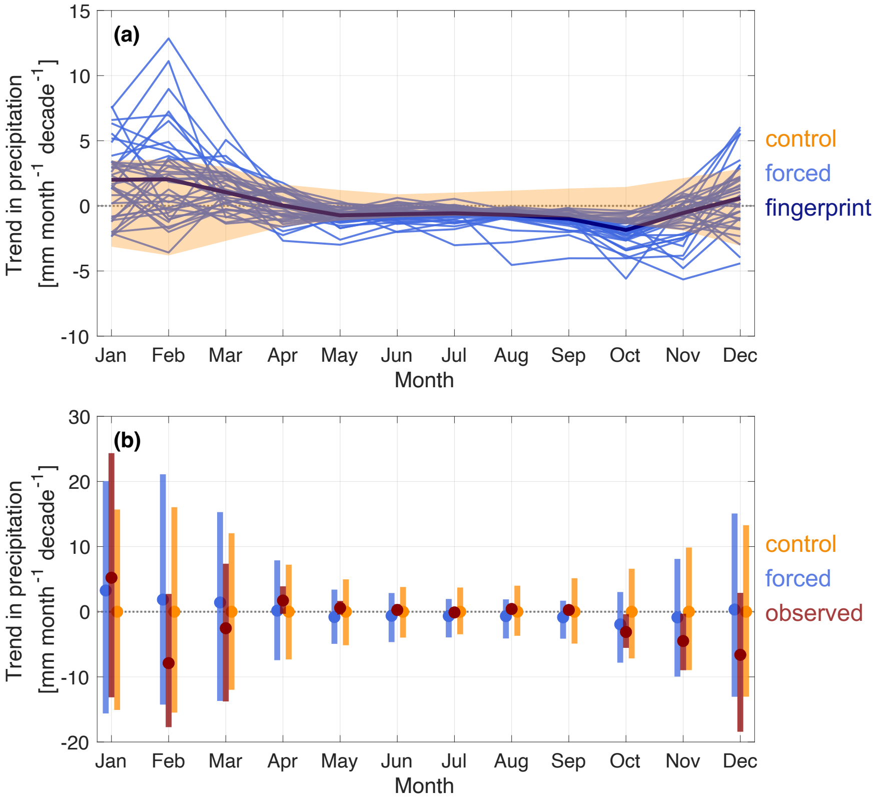

Supplementary Figure 9 Climate change fingerprint Same as Fig. 2, but using precipitation instead of soil moisture. The observed precipitation is from CHIRPS. There are 38 model ensembles with simulations of monthly precipitation available for PiControl, historical, and SSP-8.5 experiments. Precipitation simulations are from the following models and ensembles: ACCESS-CM2 (r1i1p1f1), ACCESS-ESM1-5 (r1i1p1f1), AWI-CM-1-1-MR (r1i1p1f1), BCC-CSM2-MR (r1i1p1f1), CAMS-CSM1-0 (r1i1p1f1), CanESM5-CanOE (r1i1p2f1), CanESM5 (r1i1p1f1, r1i1p2f1), CAS-ESM2-0 (r1i1p1f1), CESM2-WACCM (r1i1p1f1), CMCC-CM2-SR5 (r1i1p1f1), CMCC-ESM2 (r1i1p1f1), CNRM-CM6-1-HR (r1i1p1f2), CNRM-CM6-1 (r1i1p1f2), CNRM-ESM2-1 (r1i1p1f2), E3SM-1-1 (r1i1p1f1), EC-Earth3 (r1i1p1f1), EC-Earth3-Veg-LR (r1i1p1f1), FGOALS-f3-L (r1i1p1f1), FGOALS-g3 (r1i1p1f1), GFDL-CM4 (r1i1p1f1), GFDL-ESM4 (r1i1p1f1), GISS-E2-1-G (r1i1p3f1, r1i1p5f1), IITM-ESM (r1i1p1f1), INM-CM4-8 (r1i1p1f1), KACE-1-0-G (r1i1p1f1), KIOST-ESM (r1i1p1f1), MIROC6 (r1i1p1f1), MIROC-ES2L (r1i1p1f2), MPI-ESM1-2-HR (r1i1p1f1), MPI-ESM1-2-LR (r1i1p1f1, r2i1p1f1), MRI-ESM2-0 (r1i1p1f1, r1i2p1f1), NESM3 (r1i1p1f1), NorESM2-MM (r1i1p1f1), TaiESM1 (r1i1p1f1).

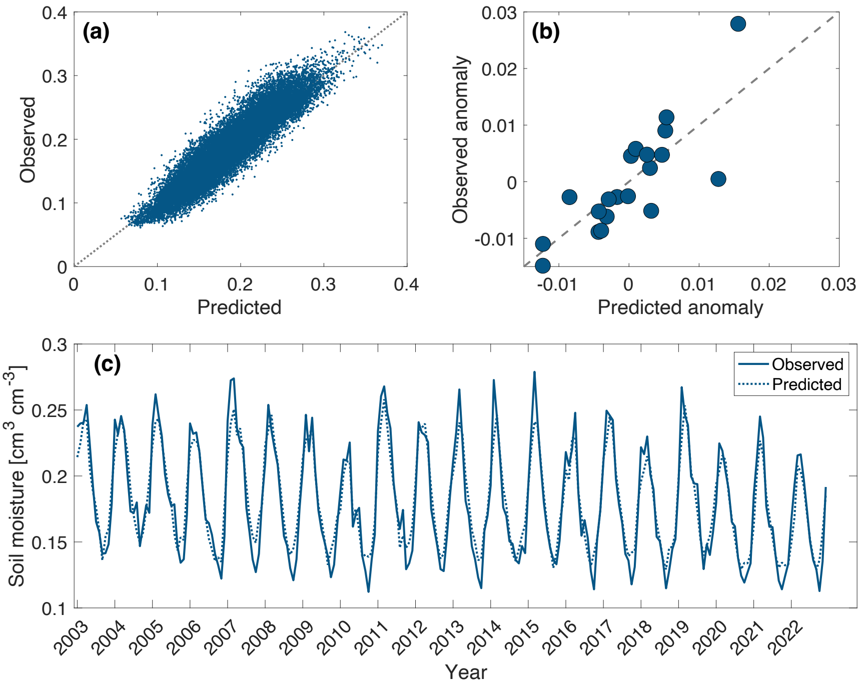

Supplementary Figure 10 Assessment of NDVI as a predictor of soil moisture from 2003 to 2022 (a) One-to-one plot of monthly soil moisture predictions and observations across all months and grid boxes in Southern Madagascar. Each point represents data from one month at one grid-box. (b) One-to-one plot of seasonal anomalies (Sep-Nov) of average soil moisture across Southern Madagascar. Anomalies are estimated as the differences between the yearly seasonal value and the average seasonal value from 2003 to 2022. Each point represents anomalies for one year. (c) Average soil moisture across Southern Madagascar from observations (solid line) and predictions (dotted line).

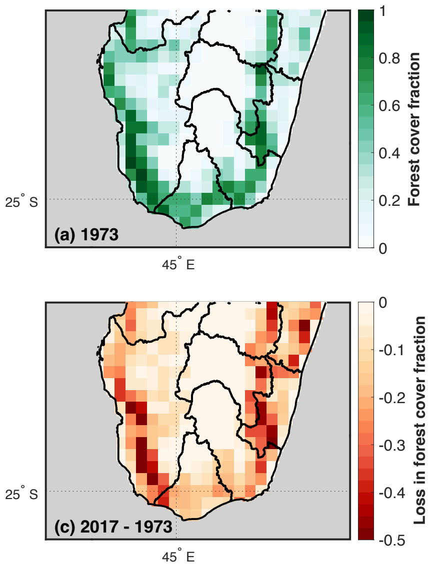

Supplementary Figure 11 Forest cover loss from 1973 to 2017 Forest cover fractions for each 0.25-degree grid box in (a) 1973 and (b) 2017. We estimate the (c) difference in forest cover fractions from 1973 to 2017, defining (d) regions with minimal deforestation as grid boxes with changes in fractions less than 0.15, which are mapped in cyan.

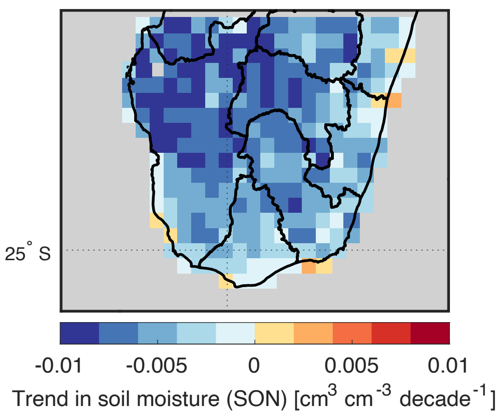

Supplementary Figure 12 Trend in proxy soil moisture Linear trends in proxy average soil moisture over the onset period (Sep-Nov) from 1982 to 2022. Trends are estimated for every 0.25-degree grid box, regardless of land use changes (Supplementary Fig. 11).

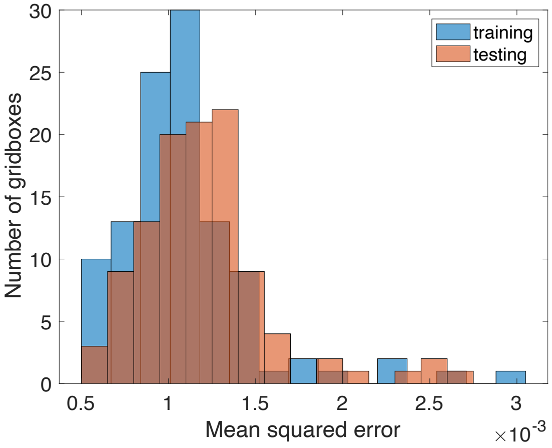

Supplementary Figure 13 Histogram of errors associated with proxy soil moisture estimates Mean squared error in Eq. 1 estimated from the training and testing subsets (see Methods). Each count in the histogram is the average mean squared error across training or testing subsets for one grid box in the undisturbed region of Southern Madagascar.

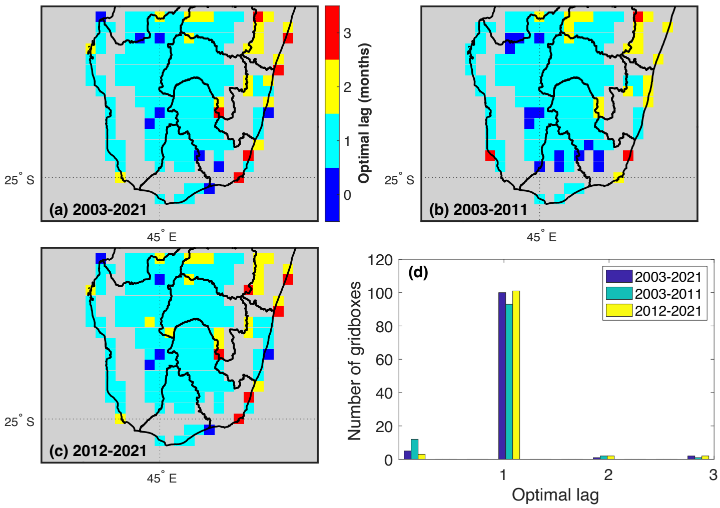

Supplementary Figure 14 Monthly lags between NDVI and soil moisture Optimal lag (monthly) between soil moisture and NDVI (with NDVI lagging soil moisture) estimating using data from (a) 2003 to 2022, (b) 2003 to 2011, and (c) 2012 to 2022. (d) A histogram of lags (months) estimated from these three time periods. Each count in the histogram is the optimal lag for one gridbox in the undisturbed region of Southern Madagascar.

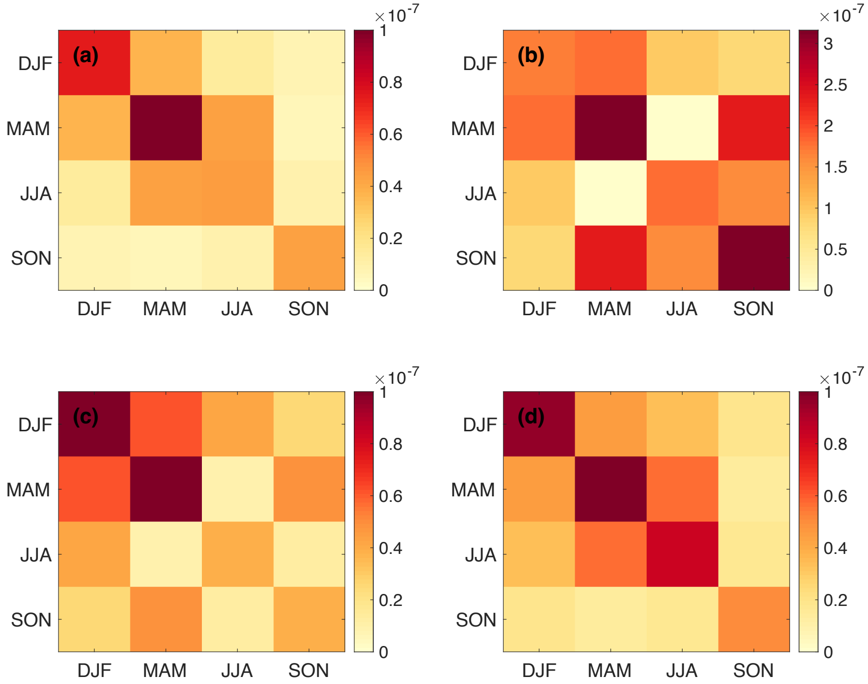

Supplementary Figure 15 Covariance between seasonal trends. Covariance matrix for seasonal trends in soil moisture in (a) control simulations and (b,c,d) forced simulations from nine CMIP6 model runs. The covariance matrices in the forced simulations are based on (b) trends from 1982 to 2022 ("Alt 1" in Supplementary Table 2), (c) trends from 1982 to 2022 and 1987 to 2027 ("Alt 2"), and (d) trends of 41-year length estimated every 5 years from 1982 to 2099 ("Alt 3"). Covariance is estimated by aggregating trends across all model runs and samples for each season. Note that the diagonal represents the variance of trends for the specified season.

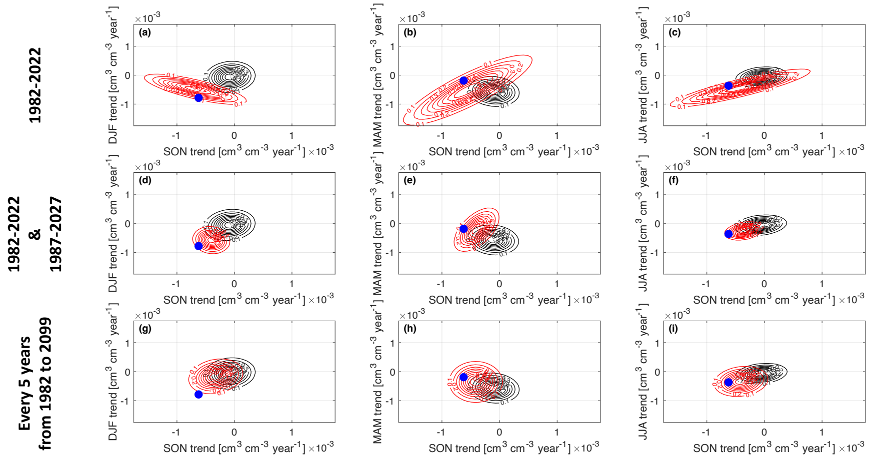

Supplementary Figure 16 Visualization of trend attribution. Slice of multivariate normal distributions (MVNs) fit to null (L_{null}; black) and alternative (L_{alt}; red) simulated trends. L_{alt} is estimated using trends from 1982 to 2022 ("Alt 1" in Supplementary Table 2) in the top row (a,b,c), trends from 1982 to 2022 and 1987 to 2027 ("Alt 2") in the middle row (d,e,f), and 41 year trends every 5-years from 1982 to 2099 ("Alt 3") in the bottom row (g,h,i). Each subplot show a slice of the four-dimensional distribution and associated probabilities of trends for two of the four season: (a,d,g) SON and DJF, (b,e,h) SON and MAM, and (c,f,i) SON and JJA. Trends in seasonal proxy soil moisture are shown in blue dots.

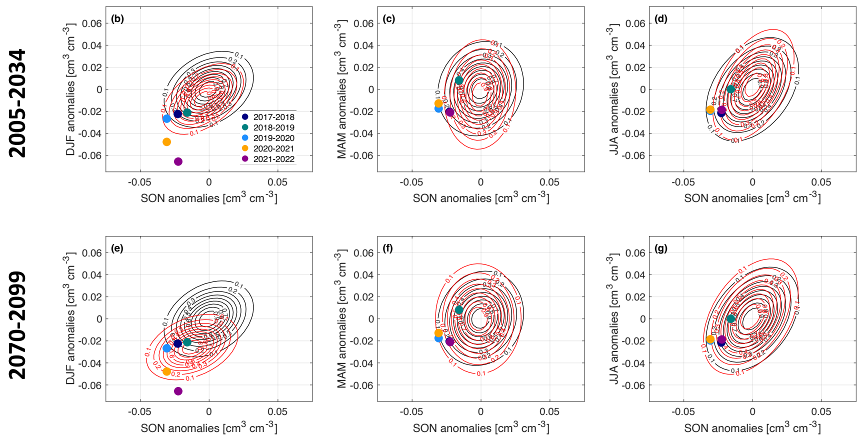

Supplementary Figure 17 Main approach for drought attribution. Slice of MVN fit to null (L_{null}; black) and alternative (L_{alt}; red) data in the drought attribution for drought years during 2017–2022 using approach 1. The top row (a,b,c) is associated with an alternative period from 2005-2034 that is centered on the drought years and the bottom row (d,e,f) an alternative period from 2070-2090. Each column shows a slice of the four-dimensional MVN of soil moisture anomalies for two of the four season: (a,d) SON and DJF, (b,e) SON and MAM, and (c,f) SON and JJA. Observed soil moisture anomalies for different drought years are indicated by dots, as indicated in the legend in subplot (a).

3 Supplementary Tables

Supplementary Table 1: **CMIP6 climate model and ensemble members**. Fig. 3 includes vertical velocity data from all listed climate model and ensemble members. The remaining analysis of soil moisture uses models and ensembles in which simulations of monthly soil moisture are available for PiControl, historical, and SSP-8.5 experiments, which are indicated with an asterisk (*). Three of the runs, which are indicated with a plus sign (+), are excluded from the analysis because of biases in the seasonal cycle of the piControl simulations (Supplementary Fig. 4).

Model	**Ensemble**
ACCESS-CM2	r1i1p1f1*, r2i1p1f1, r3i1p1f1, r4i1p1f1, r5i1p1f1
ACCESS-ESM1-5	r11i1p1f1, r12i1p1f1, r13i1p1f1, r14i1p1f1, r15i1p1f1, r16i1p1f1, r17i1p1f1, r18i1p1f1, r19i1p1f1, r20i1p1f1, r21i1p1f1, r22i1p1f1, r23i1p1f1, r24i1p1f1, r25i1p1f1, r26i1p1f1, r27i1p1f1, r28i1p1f1, r29i1p1f1, r30i1p1f1, r31i1p1f1, r32i1p1f1, r33i1p1f1, r34i1p1f1, r35i1p1f1, r36i1p1f1, r39i1p1f1, r40i1p1f1
AWI-CM-1-1-MR	r1i1p1f1
BCC-CSM2-MR	r1i1p1f1*
CAMS-CSM1-0	r1i1p1f1, r2i1p1f1
CAS-ESM2-0	r1i1p1f1, r3i1p1f1
CESM2	r10i1p1f1, r11i1p1f1, r4i1p1f1
CESM2-WACCM	r1i1p1f1*, r2i1p1f1, r3i1p1f1, r4i1p1f1, r5i1p1f1
CIESM	r1i1p1f1
CMCC-CM2-SR5	r1i1p1f1
CMCC-ESM2	r1i1p1f1
CNRM-CM6-1	r1i1p1f2, r2i1p1f2, r3i1p1f2, r4i1p1f2, r5i1p1f2, r6i1p1f2
CNRM-CM6-1-HR	r1i1p1f2
CNRM-ESM2-1	r1i1p1f2, r2i1p1f2, r3i1p1f2, r4i1p1f2, r5i1p1f2
CanESM5	r1i1p1f1*, r1i1p2f1*, r3i1p1f1, r3i1p2f1, r4i1p1f1, r4i1p2f1, r5i1p1f1, r5i1p2f1, r6i1p1f1, r6i1p2f1, r7i1p1f1, r7i1p2f1, r8i1p1f1, r8i1p2f1, r9i1p1f1, r9i1p2f1, r10i1p1f1, r10i1p2f1, r11i1p1f1, r11i1p2f1, r12i1p1f1, r12i1p2f1, r13i1p1f1, r13i1p2f1, r14i1p1f1, r14i1p2f1, r15i1p1f1, r15i1p2f1, r16i1p1f1, r16i1p2f1, r17i1p1f1, r17i1p2f1, r18i1p1f1, r18i1p2f1, r19i1p1f1, r19i1p2f1, r20i1p1f1, r20i1p2f1, r21i1p1f1, r21i1p2f1, r22i1p1f1, r22i1p2f1, r23i1p1f1, r23i1p2f1, r24i1p1f1, r24i1p2f1, r25i1p1f1, r25i1p2f1, r2i1p1f1, r2i1p2f1
CanESM5-CanOE	r1i1p2f1, r2i1p2f1, r3i1p2f1
E3SM-1-1	r1i1p1f1
EC-Earth3	r11i1p1f1*+, r13i1p1f1, r15i1p1f1, r1i1p1f1, r3i1p1f1, r4i1p1f1, r6i1p1f1, r9i1p1f1
EC-Earth3-CC	r1i1p1f1
EC-Earth3-Veg	r1i1p1f1*+, r2i1p1f1, r3i1p1f1, r4i1p1f1, r6i1p1f1, r10i1p1f1, r12i1p1f1, r14i1p1f1

EC-Earth3-Veg-LR	r1i1p1f1, r2i1p1f1, r3i1p1f1
FGOALS-f3-L	r1i1p1f1
FGOALS-g3	r1i1p1f1, r2i1p1f1, r3i1p1f1, r4i1p1f1
FIO-ESM-2-0	r1i1p1f1, r2i1p1f1, r3i1p1f1
GFDL-CM4	r1i1p1f1*
GFDL-ESM4	r1i1p1f1
GISS-E2-1-G	r1i1p3f1, r1i1p5f1, r2i1p1f2, r2i1p3f1, r3i1p1f2, r3i1p3f1, r4i1p1f2, r4i1p3f1, r5i1p1f2, r5i1p3f1
GISS-E2-1-H	r1i1p1f2, r2i1p1f2, r4i1p1f2, r5i1p1f2
HadGEM3-GC31-LL	r1i1p1f3, r2i1p1f3, r3i1p1f3
HadGEM3-GC31-MM	r1i1p1f3, r2i1p1f3, r3i1p1f3, r4i1p1f3
IITM-ESM	r1i1p1f1
INM-CM4-8	r1i1p1f1
INM-CM5-0	r1i1p1f1
IPSL-CM6A-LR	r1i1p1f1*, r2i1p1f1, r3i1p1f1, r4i1p1f1, r6i1p1f1, r14i1p1f1
KACE-1-0-G	r1i1p1f1, r2i1p1f1, r3i1p1f1
KIOST-ESM	r1i1p1f1
MIROC-ES2L	r1i1p1f2*+, r2i1p1f2, r3i1p1f2, r4i1p1f2, r5i1p1f2, r6i1p1f2, r7i1p1f2, r8i1p1f2, r9i1p1f2, r10i1p1f2
MIROC6	r1i1p1f1*, r2i1p1f1, r3i1p1f1, r4i1p1f1, r5i1p1f1, r6i1p1f1, r7i1p1f1, r8i1p1f1, r9i1p1f1, r10i1p1f1, r11i1p1f1, r12i1p1f1, r13i1p1f1, r14i1p1f1, r15i1p1f1, r16i1p1f1, r17i1p1f1, r18i1p1f1, r19i1p1f1, r20i1p1f1, r21i1p1f1, r22i1p1f1, r23i1p1f1, r24i1p1f1, r25i1p1f1, r26i1p1f1, r27i1p1f1, r28i1p1f1, r29i1p1f1, r30i1p1f1, r31i1p1f1, r32i1p1f1, r33i1p1f1, r34i1p1f1, r35i1p1f1, r36i1p1f1, r37i1p1f1, r38i1p1f1, r39i1p1f1, r40i1p1f1, r41i1p1f1, r42i1p1f1, r43i1p1f1, r44i1p1f1, r45i1p1f1, r46i1p1f1, r47i1p1f1, r48i1p1f1, r49i1p1f1, r50i1p1f1
MPI-ESM1-2-HR	r1i1p1f1, r2i1p1f1
MPI-ESM1-2-LR	r1i1p1f1, r2i1p1f1, r3i1p1f1, r4i1p1f1, r5i1p1f1, r6i1p1f1, r7i1p1f1, r8i1p1f1, r9i1p1f1, r10i1p1f1
MRI-ESM2-0	r1i2p1f1, r2i1p1f1, r3i1p1f1, r4i1p1f1, r5i1p1f1
NESM3	r1i1p1f1, r2i1p1f1
NorESM2-LM	r1i1p1f1
NorESM2-MM	r1i1p1f1
TaiESM1	r1i1p1f1
UKESM1-0-LL	r1i1p1f2*, r2i1p1f2, r3i1p1f2, r4i1p1f2, r8i1p1f2

Supplementary Table 2 Input data used to fit and evaluate the multivariate normal distributions in the attribution, including the null (x_{null}), alternative (x_{alt}), and observations data (x). The input data used to estimate to covariance (Σ) and mean (μ) are specified for the null and alternative data. For the climate model simulations, data are aggregated across all nine clime model runs (Supplementary Table 1).

Attribution	$x_{\textbf{null}}$	$x_{\textbf{alt}}$	x
Long-term trends	Covariance and mean: Seasonal trends in the control simulations, with trends of 41-year length estimated every 5 years from year 10 to 500	Covariance and mean: Alt 1: Seasonal trends in the forced simulations from 1982 to 2022; Alt 2: Seasonal trends in the forced simulations from 1982 to 2022 and 1987 to 2027; Alt 3: Seasonal trends in the forced simulations, with trends of 41-year length estimated every 5 years from 1982 to 2099	Seasonal trends in proxy soil moisture from 1982 to 2022
Drought (approach 1)	Covariance and mean: Seasonal anomalies[a] in soil moisture during the period from 1970 to 2099	Covariance and mean: Seasonal anomalies[a] in soil moisture during the period from 2005 to 2034[c]	Seasonal anomalies[b] in proxy soil moisture during the drought year, including 2018, 2019, 2020, 2021, and 2022
Drought (approach 2)	Covariance: Seasonal anomalies in soil moisture during the period from 1970 to 2099 Mean: Seasonal soil moisture estimate in 1982 via a linear trend in proxy soil moisture from 1982 to 2017	Covariance: Seasonal anomalies in soil moisture during the period from 2005 to 2034 Mean: Seasonal soil moisture estimate for the drought year via an extrapolation of the linear trend in proxy soil moisture from 1982 to 2017	Seasonal mean proxy soil moisture during the drought year, including 2018, 2019, 2020, 2021, and 2022

[a]anomalies are relative the seasonal average during the baseline, 1970-1999; [b]anomalies are relative the seasonal soil moisture estimate in 1982 via a linear trend in proxy soil moisture from 1982 to 2017; [c]this alternative period can be defined over a range of 30-year periods (Fig. 5).

Supplementary Table 3 Drought attribution. The likelihood ratio, λ, for how many times more likely x is to occur in current and future conditions relative to a climatology defined between 1970-1999 using the CMIP6 models (approach 1; "app. 1") and the CMIP6 models combined with observed trends (approach 2; "app. 2"). All evaluation are for years running from September to August. 90% confidence intervals are indicated in parentheses and reflect both the uncertainty in x and in the estimation of multivariate normal distributions. Asterisks indicate that the likelihood ratio is significant at $p < 0.01$.

	2005-2034		**2020-2049**		**2070-2099**
Drought year	**App. 1**	**App. 2**	**App. 1**	**App. 2**	**App. 1**
2017-2022	15.5 (8.5-27)*	141.1 (0.2-75310)	63.4 (32.2-122.7)*	145 (0.5-103223	28382 (4978-218210)*
2017-2021	15.1 (9.7-24.2)*	171.7 (4.7-5314)	23.4 (12.6-45.4)*	145 (5.2-4061)	615.2 (122.2-3892)*
2017-2018	1.7 (1.5-1.9)*	2.2 (1.1-4.2)	1.9 (1.6-2.2)*	2.2 (1.1-4.1)	2.7 (1.7-4.4)*
2018-2019	1.9 (1.7-2.3)*	2.8 (1.5-4.9)	1.9 (1.6-2.4)*	2.6 (1.5-4.6)	2.3 (1.5-3.8)*
2019-2020	1.9 (1.6-2.2)*	4.8 (2.3-10)*	2.1 (1.7-2.5)*	4.5 (2.2-9.3)*	4.5 (2.9-7.4)*
2020-2021	2.4 (2.1-2.8)*	5.8 (1-29.5)	3.2 (2.8-3.5)*	5.9 (1.1-29.2)	22.6 (16.6-31.6)*
2021-2022	1 (0.7-1.5)	0.9 (0-15.8)	2.7 (2.2-3.3)*	1.8 (0.1-25.8)	45.4 (35.1-59.2)*

References

[1] UN. Madagascar: Severe drought could spur world's first climate change famine (2021). URL https://news.un.org/en/story/2021/10/1103712.

[2] Harrington, L. J. *et al.* Limited role of climate change in extreme low rainfall associated with southern Madagascar food insecurity, 2019–21. *Environ. Res.: Climate* **1**, 021003 (2022) .

[3] Hersbach, H. *et al.* The ERA5 global reanalysis. *Q. J. R. Meteorol. Soc.* **146**, 1999–2049 (2020) .

[4] Funk, C. *et al.* The climate hazards infrared precipitation with stations—a new environmental record for monitoring extremes. *Sci. Data* **2**, 150066 (2015) .

[5] Randriamarolaza, L. Y. A., Enric, A., Oleg, S., M., S., Vicente-Serrano & Fernando, D.-C. Indices for daily temperature and precipitation in Madagascar, based on quality-controlled and homogenized data, 1950–2018. *Int J Climatol.* **42**, 265–288 (2021) .

[6] Randriamarolaza, L. Y. A. & Aguilar, E. Rainy season and crop calendars comparison between past (1950–2018) and future (2030–2100) in madagascar. *Meteorol. Appl.* **30**, e2146 (2023) .

[7] FEWSNET. An early start of the rainy season in the extreme south is favorable for early crop development (2020). URL https://fews.net/southern-africa/madagascar/food-security-outlook/october-2019.

[8] Kruger, L. The timing of agricultural production in hazard-prone areas to prevent losses at peak-risk periods: A case of Malawi, Madagascar and Mozambique. *Jamba: J. Disaster Risk Stud.* **8**, 179 (2016) .

[9] Roffe, S. J., Fitchett, J. M. & Curtis, C. J. Investigating changes in rainfall seasonality across South Africa: 1987–2016. *Int. J. Climatol.* **41**, E2031–E2050 (2021) .

[10] Randriamahefasoa, T. S. M. & Reason, C. J. C. Interannual variability of rainfall characteristics over southwestern Madagascar. *Theor. Appl. Climatol.* **128**, 421–437 (2017) .

[11] Xian, T. *et al.* Is Hadley Cell expanding? *Atmosphere* **12**, 1699 (2021) .

[12] Staten, P. W. *et al.* Tropical widening: From global variations to regional impacts. *Bull. Am. Meteorol. Soc.* **101**, E897–E904 (2020) .

[13] Burls, N. J. *et al.* The Cape Town "Day Zero" drought and Hadley cell expansion. *npj Clim. Atmos. Sci.* **2**, 27 (2019) .

[14] Muthige, M. S. *et al.* Projected changes in tropical cyclones over the South West Indian Ocean under different extents of global warming. *Environ. Res. Lett.* **13**, 065019 (2018) .

[15] Malherbe, J., Engelbrecht, F. A. & Landman, W. A. Projected changes in tropical cyclone climatology and landfall in the Southwest Indian Ocean region under enhanced anthropogenic forcing. *Clim. Dyn.* **40**, 2867–2886 (2013) .

[16] Brown, K. A., Yesuf, G. & Carvalho, F. *The New Natural History of Madagascar*, Ch. Assessing the quality of remaining forests on Madagascar, 113–120 (Princeton University Press, 2022).

[17] Hegerl, G. C. *et al.* Detecting greenhouse-gas-induced climate change with an optimal fingerprint method. *J. Clim.* **9**, 2281–2306 (1996) .

[18] Desbureaux, S. & Damania, R. Rain, forests and farmers: Evidence of drought induced deforestation in Madagascar and its consequences for biodiversity conservation. *Biol. Conserv.* **221**, 357–364 (2018) .

[19] Vieilledent, G. *et al.* Combining global tree cover loss data with historical national forest cover maps to look at six decades of deforestation and forest fragmentation in Madagascar. *Biol. Conserv.* **222**, 189–197 (2018) .

[20] Rigden, A. J., Golden, C. & Huybers, P. Retrospective predictions of rice and other crop production in Madagascar using soil moisture and an NDVI-based calendar from 2010–2017. *Remote Sens.* **14**, 1223 (2022) .

[21] Frappier-Brinton, T. & Lehman, S. M. The burning island: Spatiotemporal patterns of fire occurrence in Madagascar. *PLoS One* **17**, 1–17 (2022) .

[22] Lawrence, D. & Vandecar, K. Effects of tropical deforestation on climate and agriculture. *Nat. Clim. Change* **5**, 27–36 (2015) .

[23] Wright, J. S. *et al.* Rainforest-initiated wet season onset over the southern Amazon. *Proc. Natl. Acad. Sci.* **114**, 8481–8486 (2017) .

[24] Butt, N., de Oliveira, P. A. & Costa, M. H. Evidence that deforestation affects the onset of the rainy season in Rondonia, Brazil. *J. Geophys. Res. Atmos.* **116**, D11120 (2011) .

[25] Duku, C. & Hein, L. The impact of deforestation on rainfall in Africa: a data-driven assessment. *Environ. Res. Lett.* **16**, 064044 (2021) .

[26] Thompson, D. W. J. & Solomon, S. Interpretation of recent Southern Hemisphere climate change. *Science* **296**, 895–899 (2002) .

[27] Kang, S. M., Polvani, L. M., Fyfe, J. C. & Sigmond, M. Impact of polar ozone depletion on subtropical precipitation. *Science* **332**, 951–954 (2011) .

[28] Dhomse, S. S. *et al.* Estimates of ozone return dates from chemistry-climate model initiative simulations. *Atmos. Chem. Phys.* **18**, 8409–8438 (2018) .

[29] Hart, N. C. G., Reason, C. J. C. & Fauchereau, N. Cloud bands over southern Africa: seasonality, contribution to rainfall variability and modulation by the MJO. *Clim. Dyn.* **41**, 1199–1212 (2013) .

[30] James, R., Hart, N. C. G., Munday, C., Reason, C. J. C. & Washington, R. Coupled climate model simulation of tropical–extratropical cloud bands over southern Africa. *J. Clim.* **33**, 8579–8602 (2020) .

[31] Barimalala, R., Desbiolles, F., Blamey, R. C. & Reason, C. Madagascar influence on the South Indian Ocean Convergence Zone, the Mozambique Channel Trough and southern African rainfall. *Geophys. Res. Lett.* **45**, 11,380–11,389 (2018) .

[32] Dunning, C. M., Black, E. & Allan, R. P. Later wet seasons with more intense rainfall over Africa under future climate change. *J. Clim.* **31**, 9719–9738 (2018) .

[33] Tadross, M., Randriamarolaza, L., Rabefitia, Z. & Yip, Z. K. Climate change in Madagascar: recent, past and future. Tech. Rep., Climate Systems Analysis Group, National Meteorological Office (2008).

[34] Barimalala, R., Raholijao, N., Pokam, W. & Reason, C. J. C. Potential impacts of 1.5 °C, 2 °C global warming levels on temperature and rainfall over Madagascar. *Environ. Res. Lett.* **16**, 044019 (2021) .

[35] Jones, M. W. *et al.* National contributions to climate change due to historical emissions of carbon dioxide, methane, and nitrous oxide since 1850. *Sci. Data* **10**, 155 (2023) .

[36] Otto, F. E. L. *et al.* Causality and the fate of climate litigation: The role of the social superstructure narrative. *Glob. Policy* **13**, 736–750 (2022) .

[37] Tucker, C. J. *et al.* An extended AVHRR 8-km NDVI dataset compatible with MODIS and SPOT vegetation NDVI data. *Int. J. Remote Sens.* **26**, 4485–4498 (2005) .

[38] Tucker, C. J., Pinzon, J. E. & Brown, M. E. Global inventory modeling and mapping studies (ndvi 3g.v1) (2004).

[39] Pinzon, J. E. & Tucker, C. J. A non-stationary 1981–2012 AVHRR NDVI3g time series. *Remote Sens.* **6**, 6929–6960 (2014) .

[40] Dorigo, W. *et al.* ESA CCI soil moisture for improved earth system understanding: State-of-the art and future directions. *Remote Sens. Environ.* **203**, 185–215 (2017) .

[41] Gruber, A., Scanlon, T., van der Schalie, R., Wagner, W. & Dorigo, W. Evolution of the ESA CCI soil moisture climate data records and their underlying merging methodology. *Earth Syst. Sci. Data* **11**, 717–739 (2019) .

[42] Feldman, A. F. *et al.* Remotely sensed soil moisture can capture dynamics relevant to plant water uptake. *Water Resour. Res.* **59**, e2022WR033814 (2023) .

[43] Preimesberger, W., Scanlon, T., Su, C.-H., Gruber, A. & Dorigo, W. Homogenization of structural breaks in the global ESA CCI soil moisture multisatellite climate data record. *IEEE Trans. Geosci. Remote Sens.* **59**, 2845–2862 (2021) .

[44] Hansen, M. C. *et al.* High-resolution global maps of 21st-century forest cover change. *Science* **342**, 850–853 (2013) .

[45] Wang, A., Kong, X., Chen, Y. & Ma, X. Evaluation of soil moisture in CMIP6 multimodel simulations over conterminous China. *J. Geophys. Res. Atmos.* **127**, e2022JD037072 (2022) .

[46] Di Luca, A., de Elía, R. & Laprise, R. Potential for added value in precipitation simulated by high-resolution nested regional climate models and observations. *Clim. Dyn.* **38**, 1229–1247 (2012) .

[47] Stott, P. A. *et al.* Detection and attribution of climate change: a regional perspective. *Wiley Interdiscip. Rev. Clim. Change* **1**, 192–211 (2010) .

[48] Chiang, F., Greve, P., Mazdiyasni, O., Wada, Y. & AghaKouchak, A. A multivariate conditional probability ratio framework for the detection and attribution of compound climate extremes. *Geophys. Res. Lett.* **48**, e2021GL094361 (2021) .

[49] Rousseeuw, P. J. & Driessen, K. V. A fast algorithm for the minimum covariance determinant estimator. *Technometrics* **41**, 212–223 (1999) .